DFT-driven insights into X_2MgGeY_6 (X = Na, K; Y = Cl, I) perovskites for photovoltaic and optoelectronic Applications

T. Usman

Department of Physics, Qilu Institute of Technology, Jinan 250200, Shandong, P. R. China.

J. Iqbal

Institute of Physics, Gomal University, Dera Ismail Khan 29220, K.P., Pakistan.

M. Archi

Research Laboratory Physics and Sciences for Engineers (LRPSI), Poly-disciplinary Faculty, Sultan Moulay Slimane University, Beni Mellal-Morocco.

M. Yar Khan

Department of Physics, Qilu Institute of Technology, Jinan 250200, Shandong, P. R. China.

S. Ullah

Department of Physics, University of Buner 19290, KPK, Pakistan.

S. Ali Khan

School of Materials Science & Engineering, Shandong University, Jinan 25000, P. R. China.

Received 7 July 2025; accepted 17 September 2025

We present in this study a comprehensive analysis of the structural, mechanical, electronic, and optical properties of X_2MgGeY_6 (X = Na, K; Y = Cl, I) perovskite compounds via density functional theory (DFT). The analyzed structural parameters are in close agreement with the available data of the computed structures. The tolerance factor and the positive phonon frequencies in the band structures, authenticate the structural and dynamic stabilities. Analysis of electronic spectra shows that all examined compounds exhibit semiconducting characteristics, with indirect bandgap of 3.13, 1.70, 3.16 and 1.72 eV, respectively. Mechanical analysis confirmed the ionic bonding nature of these materials, as evidenced by positive Cauchy pressure values. As well, the mechanical stability criteria and elastic constants further validate their stability, anisotropy, and ductile behavior. Multiple optical parameters are analyzed including dielectric functions, absorption coefficients, optical conductivity, refractive index and related features with the findings suggest the outstanding optoelectronic performance for photodetectors and LEDs, while iodine-based compounds demonstrate superior potential for solar cell applications. Furthermore, all materials exhibited elastic, thermodynamic, and dynamical stability, confirming their feasibility for practical applications.

Keywords: DFT; double halide perovskites; solar cells; optoelectronics; phonon dispersion curves.

DOI: https://doi.org/10.31349/RevMexFis.72.021602

1. Introduction

Perovskite materials certify their worth in most practical devices. Following the discovery of calcium titanate, the perovskite structure became intriguing to researchers due to its distinctive and astonishing combinations of properties [1]. These materials are famed for their use in a variety of devices including wireless communications, LEDs, Lasers, high conductive elements, detectors for temperature, photovoltaic electrodes and cells, energy storage, gas sensors, and more [2–12]. Currently, humanity is heavily reliant on modern technology, and most practical devices in use today operate on non-renewable energy sources. Since these non-renewable energy assets are finite, scientists have realized that they will eventually be depleted. This alarming situation has prompted a shift in focus toward renewable energy. Significant progress has been made in this field over the past decade by material scientists and engineers, leading to growing optimism about a future shift away from conventional energy sources. In this context, double perovskite ($A_2BB'X_6$) halide materials (DPHM) are performing their essential role.

Semiconducting halide perovskites with narrow bandgaps are considered fascinating materials for power harvesting applications. Recently, many perovskites have been synthesized experimentally by researchers utilizing various procedures for instance solid-state reaction method, hot injection, solution processing, and hydro-thermal processing [13–16]. Since these double perovskites are now capable of being synthesized experimentally, and opens up new possibilities for their practical applications. Besides, computational researchers are striving to predicate new double perovskite compounds to assist experimentalists in saving time and reducing the consumption of chemicals. Previously, numerous sodium- and potassium-based double perovskite halides

have been predicted. $K_2ScAgCl_6$ and $Na_2ScAgCl_6$ materials have been noted for sustaining solidity in their cubic phases. Moreover, their bandgap were found to be 3.65 eV for $K_2ScAgCl_6$ and 3.63 eV for $Na_2ScAgCl_6$, and researchers insist on their execution in thermoelectric devices [17]. Recently, another group investigated the $Na_2AgBiBr_6$ compound both experimentally and computationally. After the observations, the researchers ratified that this compound has mechanical stability and a ductile nature. They reported that this material is suitable for thermoelectric and solar cell applications [18]. Another group studied $X_2GeSnCl_6$ (X = Na and K) materials, observing that these compounds have bandgaps of 2.24 eV and 2.21 eV, respectively. The research team claimed that these materials have low reflectivity in the visible range, making them adequate for sensors, solar cells, & various other optoelectronic devices [19]. Siad et al. reported a series of K_2NaInX_6 (X = F, Cl, Br, and I) compounds and observed that these materials have very low band-gaps. Based on the properties exhibited by these materials, the authors suggested that these substances are good for the applications of UV photo-detectors and solar cells [20]. Many other researchers also worked on potassium and sodium-based materials for numerous practical devices [21].

It is obvious from the above-cited literature that potassium and sodium-based materials are preferred by the research groups due to their low price, easy availability, and exhibiting numerous combinations of properties. In the present study, we also selected a group of potassium and sodium-based X_2MgGeY_6 (X = Na, K; and Y = Cl, I) double perovskites and systematically deliberated their structures, mechanical, electronic, and optical responses using a DFT approach. Moreover, we also studied the effects of replacing cation (Na and K) at the X-site and nonmetal (Cl and I) at the Y-site on the overall behaviors of the X_2MgGeY_6 compounds. This work identifies X_2MgGeY_6 and related materials as strong contenders for use in optoelectronic and solar cells technologies, providing a foundation for future experimental studies.

2. Computational details

A detailed investigation conducted with WIEN2k computational package [22] explored all structural, optical, electronic along with mechanical properties of X_2MgGeY_6(X = Na, K; Y = Cl, I) inorganic double halide perovskites via density functional theory (DFT). The calculations performed by employing the generalized gradient approximation (GGA) as formulated by Perdew, Burke, and Ernzerhof (PBE) [23]. While the GGA approach typically diminishes energy gap of the material, the Tran and Blaha modified Becke-Johnson (TB-mBj) potential [24] was also employed for enhancing the accuracy in calculating band-gap. Equation of Kohn-Sham was solved by the full potential LAPW [25] approach in combination alongside local orbitals, while examining the diverse characteristics of the titled compounds. An appropriate RMT values are selected for ensuring convergence of total energy, to prevent any loss of electronic charge from within core region of atoms. A value for RKmax is chosen as 7, where R represents the muffin-tin radius to maintain calculation accuracy, and Kmax denotes the cutoff wave vector in the plane wave expansion [26]. Meanwhile, the cutoff energy, which distinguishes the energy gap between the core and valence bands, is set to -6.0 Ry. The total energy-volumetric data served to establish the lattice parameters through Birch-Murnaghan equation of state fitting [27]. Functions of spherical harmonic are utilized within the muffin-tin sphere, with a cutoff of Lmax set to 10 and Gmax assigned a value of 12. Successively to refine the lattice parameters, this value was subsequently abridged by 3.5%. We set in self-consistent field (scf) computations the convergence criterion for energy and charge at 0.001 Ry along with 0.00001e, correspondingly. This calculation relied on the Monkhorst-Pack [28] k-point mesh design with $10 \times 10 \times 10$ k-mesh to address the Brillouin zone using 2000 k-points. One can use the IRelast package [29] to determine the mechanical characteristics of the titled DPHM, for instance, their elastic constants, which provide insight into their stiffness and structural stability. For the computation of phonon dispersion, the Castep code [30] is utilized, which is essential for understanding the thermodynamic behavior of the titled DPHM.

3. Results and discussion

3.1. Structural parameters

Evaluating geometrical properties of the studied materials is a crucial aspect of DFT analysis, as it lays the foundation for accurately determining additional physical characteristics, for instance electronic and optical characteristics. The optimized crystal configurations of X_2MgGeY_6 (X = Na, K; Y = Cl, I) double perovskite halides, belonging to the space group Fm-3m (No. 225), are illustrated in Fig. 1a)-1d). The atoms in the presently studied compounds were settled at the lattice positions in their structures as depicted in Fig. 1. DFT approach is utilized to examine the unit cell total energy with respect to volume for X_2MgGeY_6, which is then fitted the data to equation of state Birch-Murnaghan [27]. Subsequent to the fitting process, extract values for its bulk modulus (Bo in GPa), lattice constants (ao in Å), energy (Eo in Ry) and volume (Vo in $Å^3$), as summarized in Table I. The findings divulge a clear trend of increasing lattice parameters as chlorine is progressively substituted with iodine. Such an increase results from the larger ionic size of iodine, leading to an expansion of the unit cells.

Also, the cell volume follows an analogous pattern to the lattice parameters, increasing as the ionic number of halogen rises. For each compound, optimization of energy vs volume curve was achieved by reducing total energy relative to unit cell volume and fitting results to the Birch-Murnaghan equation, as illustrated in Fig. 2. Furthermore, it was realized that both at X or Y positions the replacement of smaller ionic radii element with the larger ionic radii element caused a notable enhancement in both a_o and V_o for the given compounds.

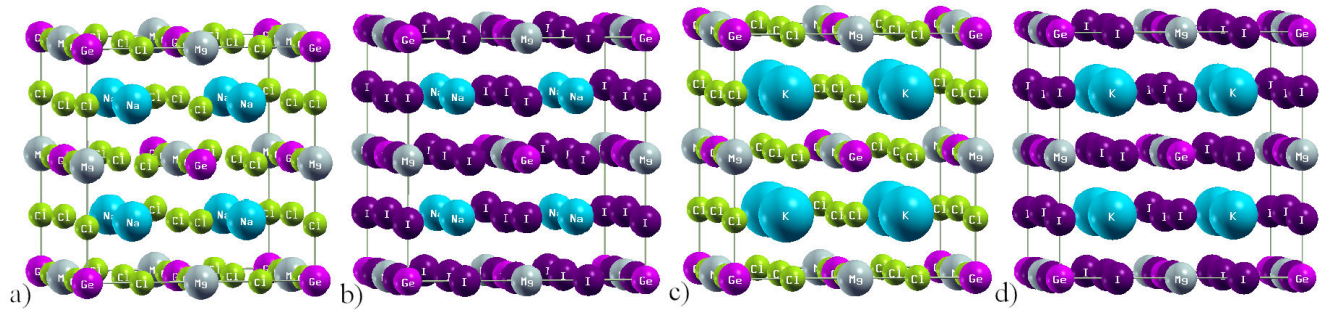

FIGURE 1. Computed optimized structures of the X_2MgGeY_6 (X = Na, K; Y = Cl, I) compounds.

TABLE I. Computed tolerance factor (t_F), lattice parameter (a_0), volume (V_0), bulk modulus (B_o), total energy (E_0), and formation energy (E_F) of X_2MgGeY_6 (X = Na, K; Y = Cl, I) compounds.

Parameters	$Na_2MgGeCl_6$	Na_2MgGeI_6	$K_2MgGeCl_6$	K_2MgGeI_6
t_F	0.82	0.81	0.93	0.90
a_o (Å)	10.39	11.87	10.48	11.91
E_0 (Ry)	-10787	-90668	-12546	-92436
V_0 (Å^3)	1893.73	2818.52	1939.78	2847.36
B_0 (GPa)	26.68	16.82	26.51	18.85
E_f (eVatom)	-2.15	-1.27	-2.27	-1.09

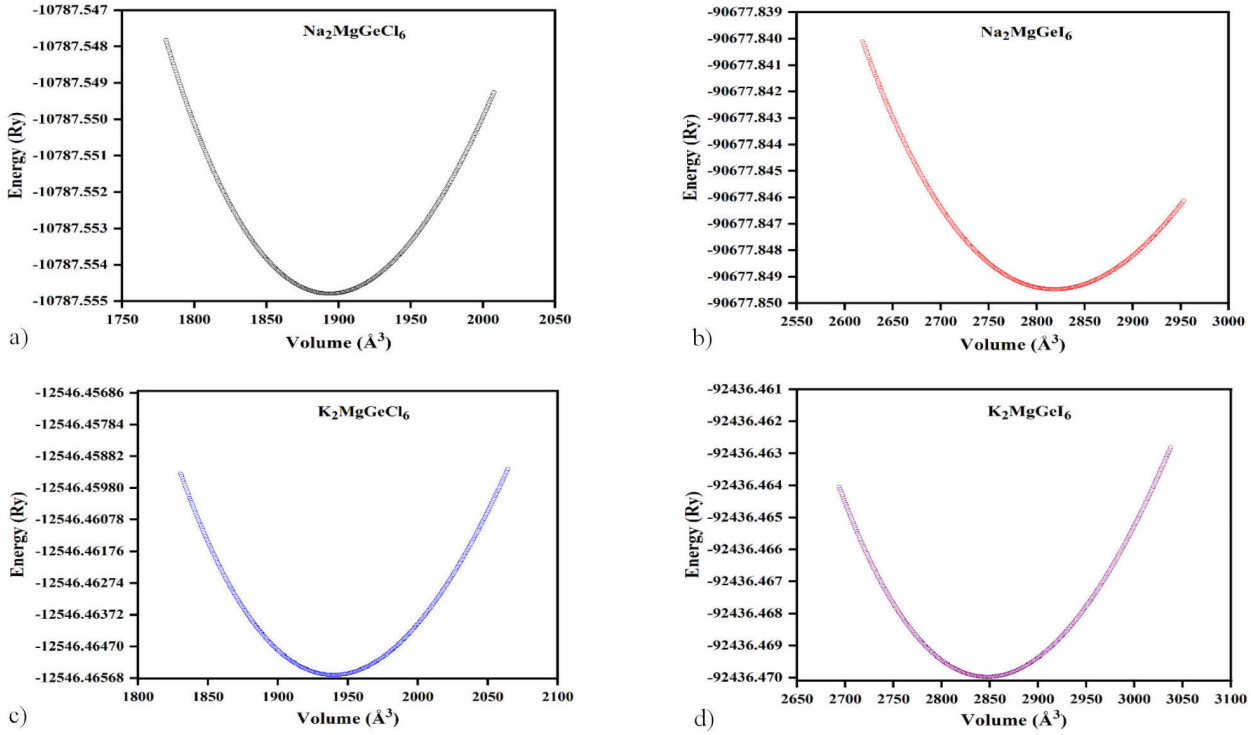

FIGURE 2. Resultant E vs V optimization plots of X_2MgGeY_6 (X = Na, K; Y = Cl, I) materials.

As, the structure compactness reduces with inducing elements having larger ionic radii, the same phenomenon was observed in the studied materials, where the B_o values were detected to move towards lesser values as the elements at X or Y positions were replaced with elements having higher ionic radii. Moreover, the B_o values were seen to move towards lower values with increasing the lattice constant a_o values for the investigated materials. Evaluating the given

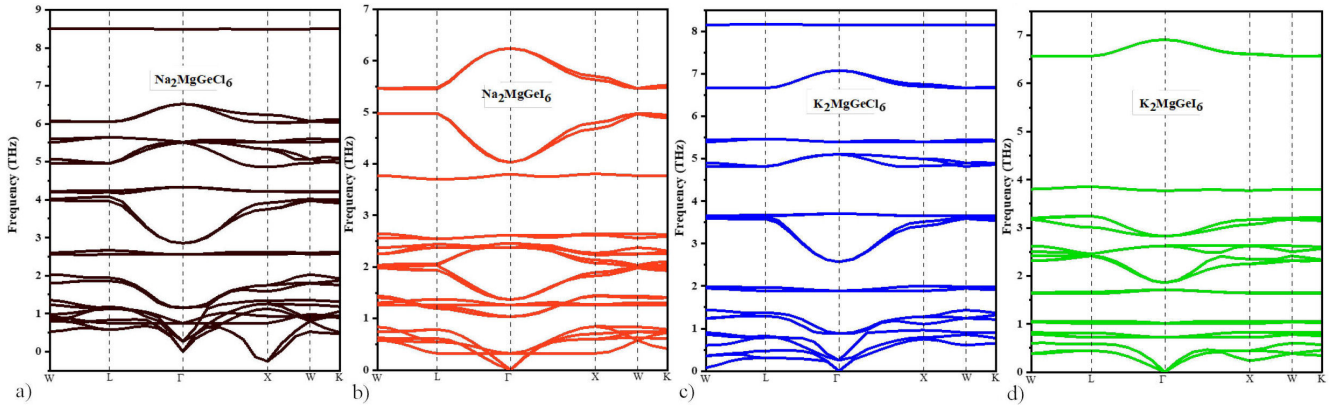

FIGURE 3. Phonon dispersion curves of X_2MgGeY_6 (X = Na, K; Y = Cl, I) perovskites.

material's tolerance factor (t_F) is essential for confirming compound structural stability. One can assess structural stability, using the relation:

$$t_F = \frac{r_X + r_Y}{\sqrt{2}\,(r_{\text{MgGe}} + r_Y\,)}. \tag{1}$$

This equation incorporates ionic radii of Na/K, Mg/Ge, and Cl/I denoted as r_X, r_{MgGe}, and r_Y, respectively. The computed tolerance factors for X_2MgGeY_6 (X = Na, K; Y = Cl, I) turn out to be 0.82, 0.81, 0.93, and 0.90, listed in Table I, which is consistent with the stability range for cubic perovskite structures [31, 32]. An additional critical parameter for the thermodynamic stabilities of the tilted compounds is the formation energy "E_F", which was calculated using the relation:

$$E_F = E_{\text{Na}_2/k_2(\text{MgGe})\text{Cl}_6/\text{I}_6} - (2E_{\text{Na/K}} + E_{\text{Mg}} + E_{\text{Ge}} + 6E_{\text{Cl/I}}). \tag{2}$$

where in this context $E_{\text{Na}_2/k_2(\text{MgGe})\text{Cl}_6/\text{I}_6}$ represents total energy of X_2MgGeY_6 at ground-state, and $E_{\text{Na/K}}$, E_{MgGe}, and E_Y denote energies at ground-state of the given atoms in their bulk forms. The calculated formation energies for X_2MgGeY_6 are listed in Table I, demonstrating the thermodynamic stability of these compounds. The negative values confirm exothermic formation reaction.

Lastly, to examine the lattice dynamics in the titled compounds, we calculated their phonon dispersion curves using the finite displacement method [33]. Castep code was employed for the phonon calculations with a wave vector spacing of 0.15 $Å^{-1}$ [34]. From Fig. 3, it is evident that the curves of phonon dispersion acquired for all the studied substances remain in the positive range and did not cross the zero line. However, only $Na_2MgGeCl_6$ compound phonon curves were seen to cross a bit the zero line a bit, acquiring negative frequencies. This indicates that the $Na_2MgGeCl_6$ compound shows slight instability in specific vibrational modes. These behaviors authenticate the structure stability of the X_2MgGeY_6 (X = Na, K; and Y = Cl, I) double perovskites.

3.2. Electronic behaviors

The applications of a material primarily rely on its electronic characteristics. A study on the band structure combined with total density of states (TDOS) and partial density of states (PDOS) of X_2MgGeY_6(X = Na, K; and Y = Cl, I) compounds delivered essential information about their electronic characteristics. The high-symmetry direction band structure information is presented in Fig. 4. From the computed band structures, it is evident that the Fermi levels are not crossed by any of the investigated materials. Furthermore, band spectra indicates that X_2MgGeY_6 compounds exhibit an indirect

TABLE II. Bandgaps of the X_2MgGeY_6 (X = Na, K; Y = Cl, I) materials and some previously reported materials.

S. No	Compound	Method	Band gap (eV)	References
1	$Na_2MgGeCl_6$	TB-mBJ	3.13	This work
2	Na_2MgGeI_6	TB-mBJ	1.70	This work
3	$K_2MgGeCl_6$	TB-mBJ	3.16	This work
4	K_2MgGeI_6	TB-mBJ	1.72	This work
5	$K_2ScAgCl_6$	GGA	3.65	[17]
6	$Na_2ScAgCl_6$	GGA	3.63	[17]
7	$Na_2AgBiBr_6$	Experimental	2.6	[18]
8	Na_2TeX_6 (X = Cl, Br, I)	GGA-PBE	3.15, 2.54, 1.85	[35]
9	Na_2AgSbX_6 (X= F, Cl, Br, and I)	PBE-GGA	3.986, 2.9, 2.3, 1.27	[36]

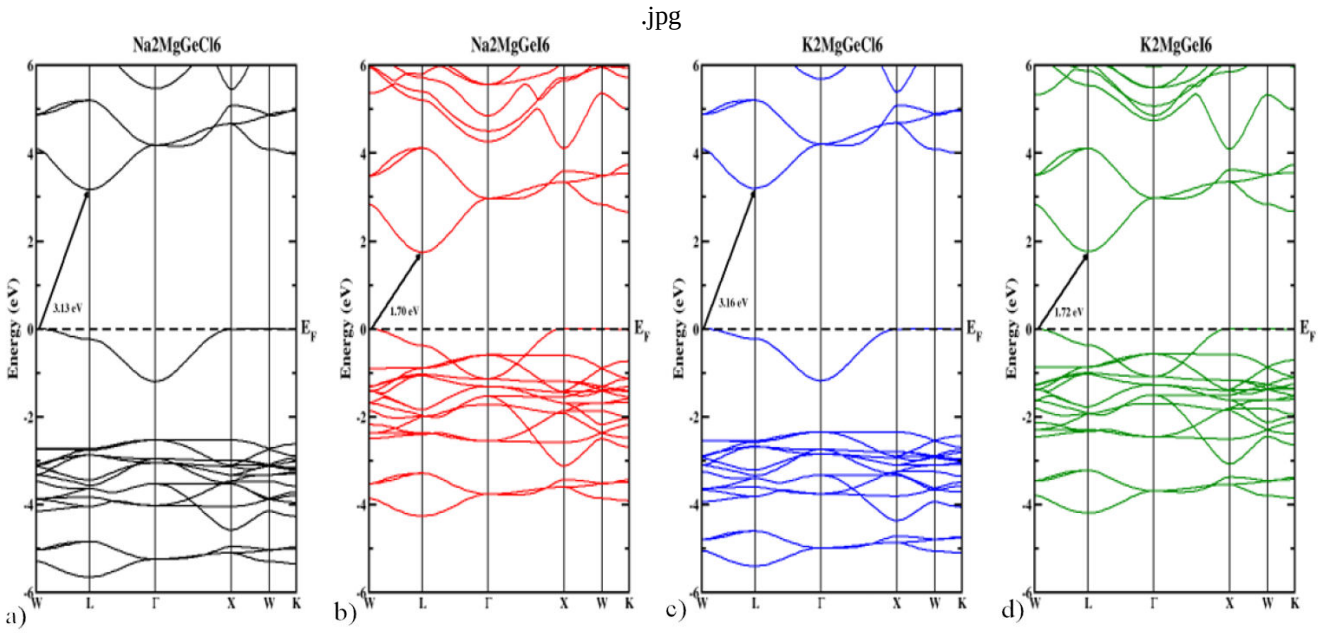

FIGURE 4. Computed band structures of X_2MgGeY_6 (X = Na, K; Y = Cl, I) compounds.

bandgap formation that presents maximum and minimum points of valence and conduction bands at the W-L symmetry points.

This characteristic of all the substances signifies that they are semiconducting. The computed values of their indirect bandgap (E_g) were 3.13 eV, 1.70 eV, 3.16 eV, and 1.72 eV for $Na_2MgGeCl_6$, Na_2MgGeI_6, $K_2MgGeCl_6$, and K_2MgGeI_6, respectively. Further analysis shows that with a rise in atomic number from Cl to I, the bandgap decreases. The acquired E_g values for the studied materials, along with the other previously reported materials, are shown in Table II. The computed E_g values for these materials signify their feasibility within optoelectronic technologies [35, 36]. The plots in Fig. 4 demonstrate that band shifting effects occur through the Cl to I movement, and it results in conduction and valence band movements toward the Fermi level, while the lower valence bands relocate identically. This shift arises due to the increased electron population in these energy regions along with the progressive occupation of electronic levels close to the Fermi energy.

To get further insight, one can accomplish an analysis of the density of states total as well partial to elucidate the nature of X_2MgGeY_6 electronic bandgap, as illustrated in Fig. 5. The TDOS structural characteristics maintain consistency between all compounds, yet the bands relocate closer to the Fermi energy. A noticeable shift occurs while moving from chlorine to iodine, because of increased atomic size, together with the rising electron count within the halide ions. This analysis proves the semiconducting behavior of the given compounds since it shows no states at the Fermi level, confirming the predicted electronic band spectra shown in Fig. 4. Based on various bands, the total and partial density of states can be categorized in two distinct areas. Figure 5 illustrates

TABLE III. Effective masses of electrons (me) and holes (mh) achieved for X_2MgGeY_6 (X = Na, K; Y = Cl, I) materials.

S. No	Compound	m_e	m_h
1	$Na_2MgGeCl_6$	0.12	1.22
2	Na_2MgGeI_6	0.078	0.19
3	$K_2MgGeCl_6$	0.125	1.23
4	K_2MgGeI_6	0.079	0.20

the contributions of different states within these bands. The initial region, spanning from about -5.0 to 0 eV, corresponds to the valence band, predominantly influenced by the Cl-tot and Ge-tot orbitals, where these states play significant roles in their respective compounds. The conduction band of X_2MgGeY_6 begins just beyond the Fermi level, with its lower segment close to the Fermi level, which is primarily governed by the Ge-tot orbital and its hybridized state with the Cl/I-tot orbital, along with a small contribution of Mg-tot. PDOS patterns signify that the non-metals (chlorine and iodine) contribute significantly to the VB. In the CB, germanium was also observed to be active alongside the nonmetals. Overall, from band and density of state calculations, these findings indicate that X_2MgGeY_6(X = Na, K; and Y = Cl, I) compounds could be highly suitable for optoelectronic and photovoltaic applications. In order to determine the transport properties of X_2MgGeY_6 (X = Na, K; and Y = Cl, I) materials, we calculated the effective masses of holes (mh) and electrons (me), and their computed values are shown in Table III. The electron's effective masses for the titled compounds were calculated from the conduction band bottom; however, for the effective masses of holes, we took the valance band top, and the following approximation was utilized [37].

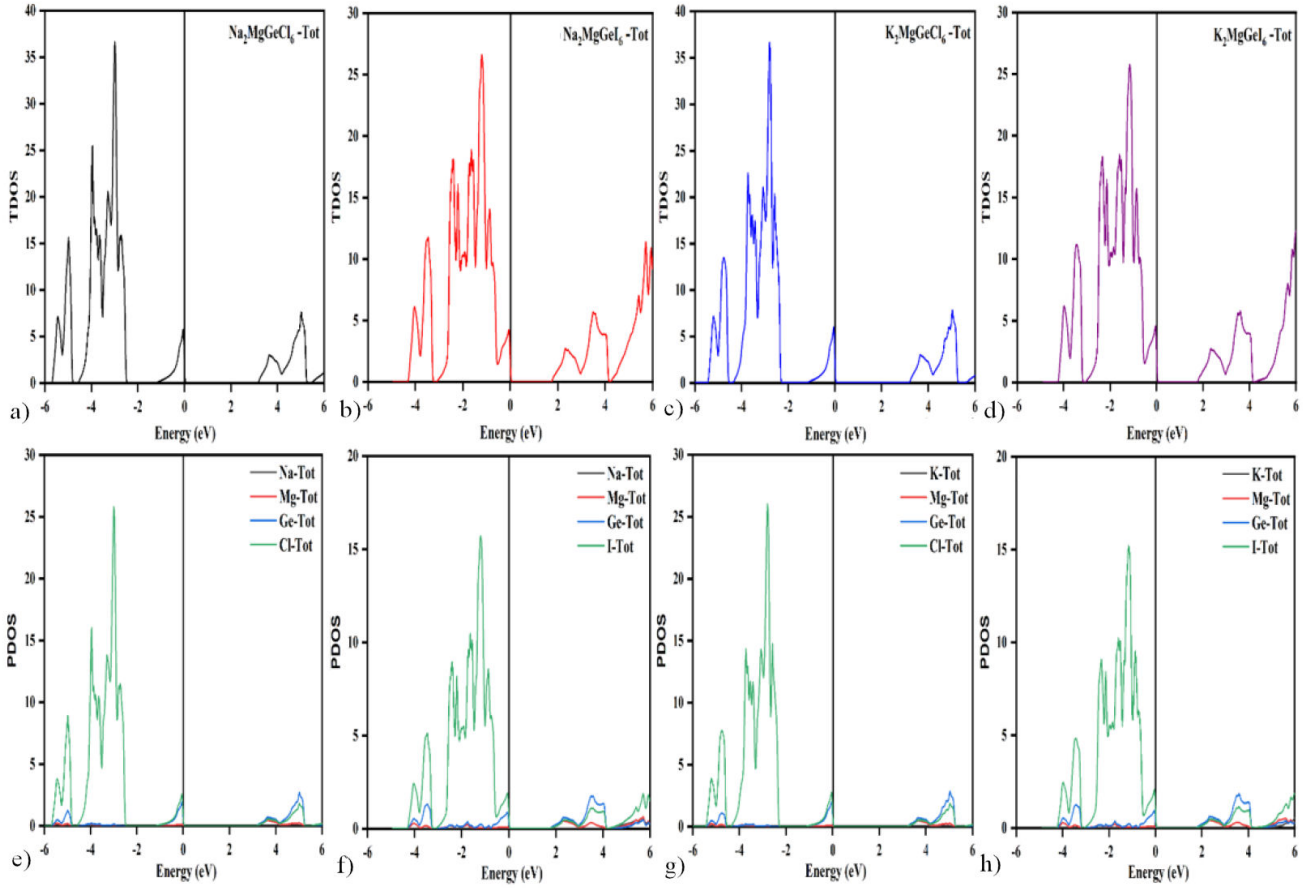

FIGURE 5. Optimized patterns of PDOS and TDOS of X_2MgGeY_6 (X = Na, K; Y = Cl, I) compounds.

$$m_{e,h} = \hbar^2 \left[\frac{\partial^2 \mathcal{E}(k)}{\partial k^2} \right]^{-1}, \tag{3}$$

where $\mathcal{E}(k)$ and *k* in Eq. (3), are the band edge eigen values and wave vector, respectively.

From the achieved results of the effective masses, it is clear that the electron's effective masses are quite lower than that of the holes, and this property signifies that the titled materials are N-type semiconductors [38]. Moreover, it has been reported that perovskite materials having less effective masses possess higher mobility, which improves transport characteristics and reduces the possibility of recombination in such compounds, signifying the suitability of such compounds for solar cell applications [39, 40]. In the presently studied materials, I-based materials possess much lower effective masses and ensure their solidity for solar cell applications.

3.3. Mechanical properties

To substantiate the structural stability under applied strain, we elaborated the three fundamental constants of elasticity for the X_2MgGeY_6(X = Na, K; and Y = Cl, I) compounds. For any crystal with a cubic structure, only three elastic constants (denoted as C_{11}, C_{12}, and C_{44}) are required to resolve all the comprehensive mechanical parameters of the structure. These computed elastic constants must accomplish the Born stability criteria, which include: $2C_{12} + C_{11}$, both C_{11} and $C_{44} > 0$, $B > C_{12}$ while less than C_{11}, and $0 < C_{11} - C_{12}$, to ensure mechanical stability [41].

From a comparative analysis of the computed constants, it was observed that the placement of iodine at the "Y" position results in lower values of the elastic constants than the materials having chlorine at the "Y". Furthermore, based on the results of Young's modulus (E), bulk modulus (B), and shear modulus (G) for the given compounds, it was concluded that the Cl-based materials exhibit superior mechanical stability compared to the I-based materials. Both $Na_2MgGeCl_6$ and $K_2MgGeCl_6$ demonstrate higher computed values for all three investigated moduli, signifying their rigidity nature. Using Eq. (4), we ascertained the Cauchy pressure "C_p" values to determine the bond nature in these studied compounds [42]. A $+ve$ value of C_p corresponds to ionic bonding, while a $-ve$ value of C_p indicates covalent bonding in the material. From Table IV, it is obvious that all the currently investigated substances have positive C_p values, confirming their ionic bonding nature.

$$C_p = C_{12} - C_{44}. \tag{4}$$

TABLE IV. Basic elastic constants and mechanical parameters of X_2MgGeY_6 (X = Na, K; Y = Cl, I) compounds.

Parameters	$Na_2MgGeCl_6$	Na_2MgGeI_6	$K_2MgGeCl_6$	K_2MgGeI_6
C_{11} (GPa)	54.57	34.32	54.10	36.32
C_{12} (GPa)	13.87	9.19	14.09	9.15
C_{44} (GPa)	7.82	6.18	9.12	6.26
E (GPa)	33.30	22.48	34.73	23.60
B (GPa)	27.44	17.57	27.43	18.21
G (GPa)	11.60	8.25	12.57	8.59
C_p	6.05	3.01	4.97	2.89
B/G	2.37	2.13	2.18	2.12
V	0.30	0.287	0.289	0.284
A	0.384	0.492	0.456	0.461

Materials are normally, categorized into two groups: brittle and ductile. These behaviors of material can be validated using their respective Pugh's "B/G" ratios and Poisson's "V" ratios. If the material B/G ratio is greater than 1.75, it exhibits ductile behaviors; otherwise, it is considered brittle. Similarly, "0.26" is the Poisson's ratio threshold value, which separates ductile materials from brittle ones [41,43]. Table IV represents the computed B/G and V values for X_2MgGeY_6 (X = Na, K; and Y = Cl, I) compounds. All the investigated substances display higher computed values of B/G and V than 1.75 and 0.26, respectively, confirming their ductile behaviors. Additionally, the Zener anisotropic "A_z" factor was also determined for all the current materials, which intensifies their anisotropic behaviors. Only materials which possess specifically "A_z = 1" are regarded as isotropic materials [44].

3.4. Optical behaviors

Material optical characteristics study empowers researchers to investigate electromagnetic radiation interaction with various substances. The X_2MgGeY_6 (X = Na, K; and Y = Cl, I) perovskites significance in optoelectronic devices was examined by their interactions with incident photons within range of $0 - 40$ eV. The linear response of the material to the incident photons is elucidated by its complex dielectric function, represented by $\varepsilon(\omega)$. This is a complex quantity, which can be mathematically described by the following equation of Ehrenreich & Cohen's [45].

$$\varepsilon(\omega) = \varepsilon_1(\omega) + i\varepsilon_2(\omega), \tag{5}$$

where $\varepsilon_1(\omega)$ in the aforementioned equation is termed the real component of $\varepsilon(\omega).\varepsilon_1(\omega)$ is entirely accountable for the irregular dispersion and electronic polarization that take place inside the material as a result of the incident photons, whereas $\varepsilon_2(\omega)$, the imaginary component, accounts for the absorption of radiations. The resultant values of $\varepsilon_1(\omega)$ and $\varepsilon_2(\omega)$ for the titled materials are graphed as a function of incident photons in Fig. 6a), 6b). Notably, the computed values of $\varepsilon_1(\omega)$ for $Na_2MgGeCl_6$ and $K_2MgGeCl_6$ at 0 energy are 2.88 and 2.96, respectively, while both Na_2MgGeI_6 and K_2MgGeI_6 showed

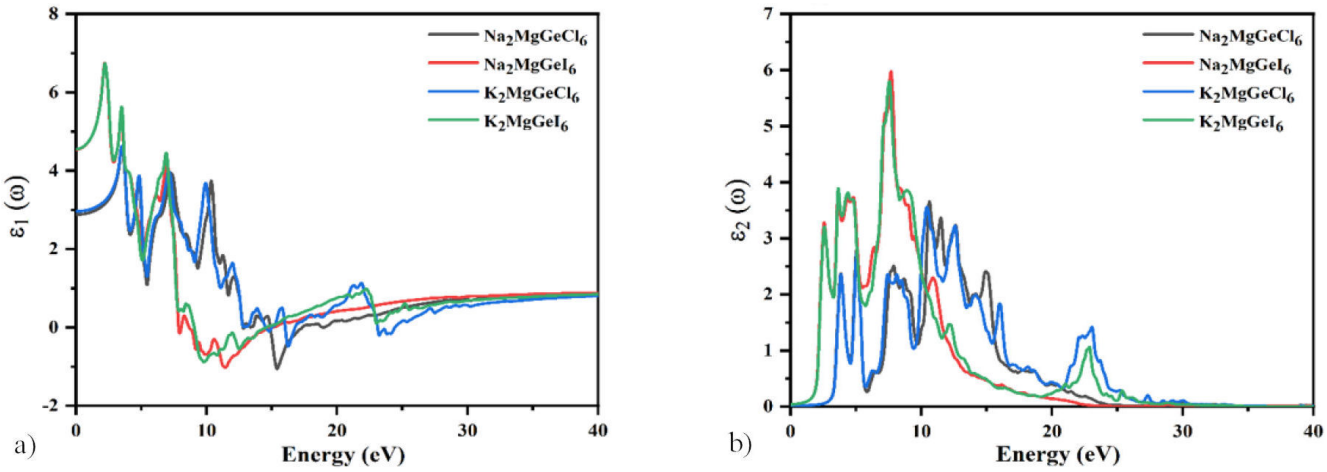

FIGURE 6. Computed patterns of a) Real components b) Imaginary components for the X_2MgGeY_6 (X = Na, K; Y = Cl, I) materials.

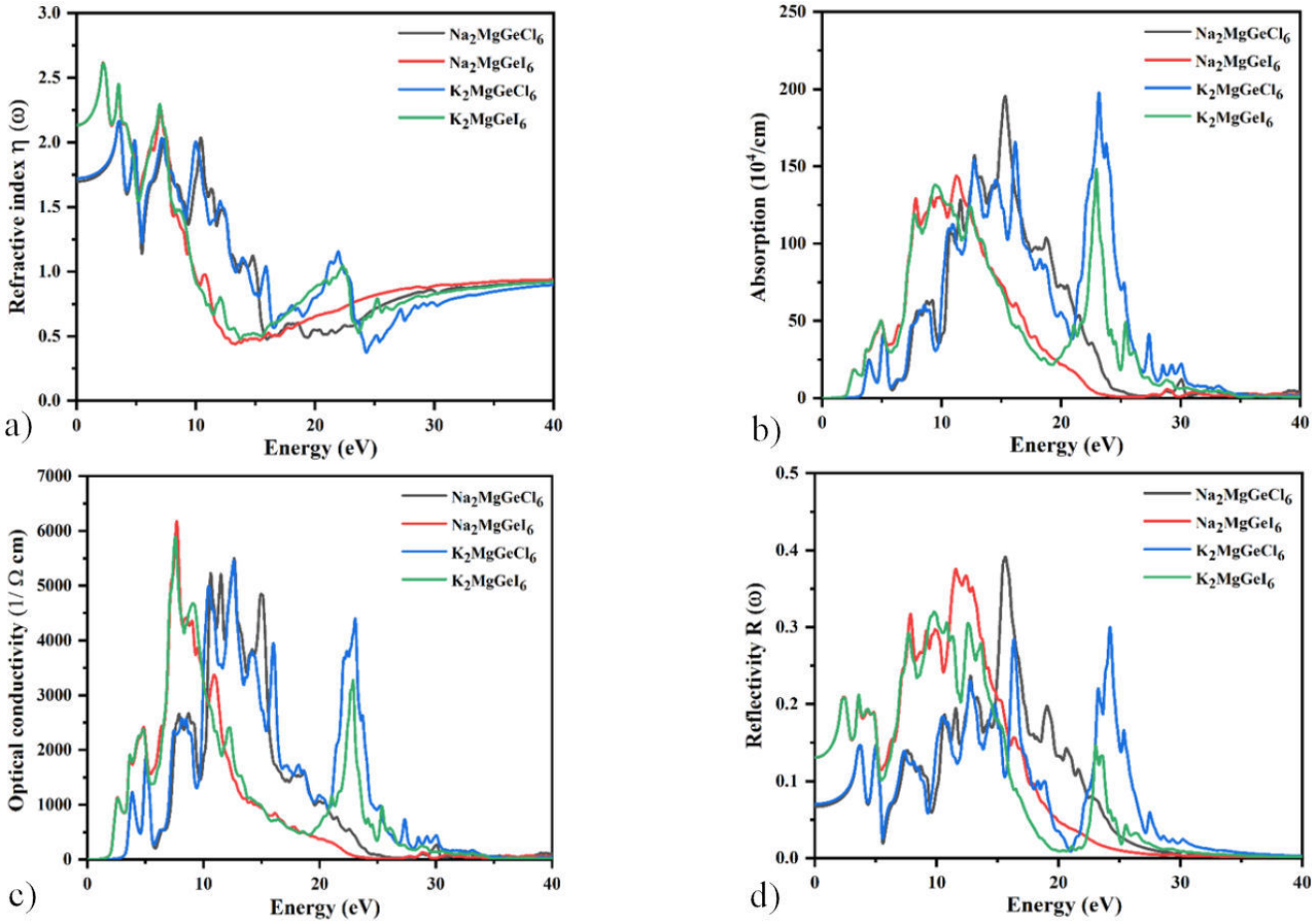

FIGURE 7. Computed patterns of optical parameters for X_2MgGeY_6 (X = Na, K; Y = Cl, I) materials.

almost the same $\varepsilon_1(0)$ value of 4.55. According to Penn's model {*i.e.*, $\varepsilon_1(0) = 1 + (h\omega_p/E_g)_2$}, those compounds that exhibit smaller E_g values permit easier electronic excitation, causing significant polarizability and thus yielding higher values of $\varepsilon_1(0)$ [46].The computed values of $\varepsilon_1(0)$ for the studied compounds show an inverse relationship with their bandgap values, which supports Penn's model.

Moreover, $\varepsilon_1(\omega)$ values surged with the initial rise in photon energy levels and achieved many peak values for all the titled materials in the 2-10 eV of photon energy. These achieved peaks of $\varepsilon_1(\omega)$ indicate the absorption behavior of these materials, highlighting the strong interaction between photons and matter [47]. However, a further increase in the photon energy causes a decline in the $\varepsilon_1(\omega)$ curves. Materials with higher computed values of $\varepsilon_1(0)$, also demonstrated a tendency to reflect photons by crossing the zero line at lower energies than others [46]. Furthermore, the computed values of $\varepsilon_2(\omega)$ remain zero for the incident photons with energies less than the bandgap of the materials. As the photon energy reaches the respective bandgap values of the titled materials, the $\varepsilon_2(\omega)$ computed values rise sharply. Notably, only Na_2MgGeI_6 and K_2MgGeI_6 materials demonstrate their foremost peaks in the visible energy (VE) range, with computed values of 3.20 & 3.27, respectively for the same photon energy of 2.57 eV. However, all the titled materials respond to photons in the ultraviolet (UV) range, with the topmost values of $\varepsilon_2(\omega)$ in the UV range achieved by materials with higher bandgap values among the studied compounds.

The computed values of the refractive index $\eta(\omega)$ in the energy range of 0-40 for the titled materials were observed and plotted in Fig. 7a). Several factors, including group velocity, composition of the material, and the wavelength of the incident waves, can affect this crucial property $\eta(\omega)$. The relation $\varepsilon_1(0) = \eta_0^2$ was accomplished by all the titled compounds computed values of $\eta(\omega)$ and $\varepsilon_1(\omega)$ at zero frequency [48]. The achieved less static computed values of $\eta(\omega)$ for the titled materials elicit them worthy for solar cells, as such materials exhibit negligible reflectivity [49]. The I-based materials acquired the supreme computed values of $\eta(\omega)$ in the VE range, while the Cl-based materials dominated in the UV range. For any semiconducting material, the extent of engrossing the light energy is described by the absorption $\alpha(\omega)$ component. Since in semiconducting materials, electronic transitions do not occur from the VB to the CB for photons with energy E_g, the titled materials showed straight lines along the x-axis for the initial photons energies, as demonstrated in Fig. 7b). However, all the titled materials displayed growth in the $\alpha(\omega)$ values for photons with

energy $\geq E_g$. Among the investigated materials, only the I-based materials presented $\alpha(\omega)$ peaks in the VE range. In the UV range, all the investigated materials showed intense peaks of $\alpha(\omega)$, with $K_2MgGeCl_6$ showing the highest peak of 197.80×10^4 cm^{-1}. The lowest value of $\alpha(\omega)$ was recorded for the Na_2MgGeI_6 compound as 143.90×10^4 cm^{-1} in the UV range.

The term optical conductivity $\alpha(\omega)$ refers to a material's ability to conduct electrons due to photon interaction. Initially, the $\alpha(\omega)$ of the titled compounds remains insensitive to lower energy radiations; however, as the radiation energy reaches the activation energy of each compound, their computed $\alpha(\omega)$ values begin to increase. The earliest $\alpha(\omega)$ peaks for the I-based compounds were observed in the VE range, and the highest computed values of 1140 and 1120 $(\Omega.m)^{-1}$ were recorded for Na_2MgGeI_6 and K_2MgGeI_6, respectively. Nevertheless, all the titled materials own the electronic conduction feature in the UV range, as confirmed in Fig. 7c). Na_2MgGeI_6 compound, with a $\alpha(\omega)$ value of 6178 $(\Omega.m)^{-1}$ at a radiation energy of 7.68 eV, holds the leading position among the investigated titled materials. While, $K_2MgGeCl_6$, $Na_2MgGeCl_6$, and K_2MgGeI_6 acquired computed $\alpha(\omega)$ values of 5489, 5499, and 5897 $(\Omega.m)^4-1$, respectively, in the UV range. In addition to exhibiting high $\alpha(\omega)$ values, these titled materials also showed quite low computed values of reflectivity $R(\omega)$, as illustrated in 7(d). Na_2MgGeI_6 and K_2MgGeI_6 show $R(\omega)$ values of 0.21 in the VE range, while in the UV range, the $R(\omega)$ values for all the investigated materials fall between 0.3-0.4.

After a thorough investigation of the optical characteristics of the titled materials, it became comprehensible that only the I-based materials have the liability for solar cell applications, while all the titled materials show suitability for optoelectronic appliances, including photodetectors, LEDs, and more.

4. Conclusion

In this computational work, the WIEN2k software was utilized to perform all calculations on the X_2MgGeY_6 (X = Na, K; and Y = Cl, I) compounds, employing the full-potential linearized augmented plane wave method. The values of the tolerance factor (t_F) were determined to be 0.82, 0.81, 0.93, and 0.90 for $Na_2MgGeCl_6$, Na_2MgGeI_6, $K_2MgGeCl_6$, and K_2MgGeI_6, respectively, all of which validate the condition of Goldschmidt. Phonon dispersion and formation energy results ensure the dynamical and thermal stabilities of the given materials. The absence of negative frequencies in the phonon curves confirms their structural stability, as no unstable vibrational modes were detected for all the studied materials except a bit for $Na_2MgGeCl_6$. Formation energy calculation revealed that all the investigated compounds possess significantly negative values, highlighting their thermodynamic stability and exothermic formation reaction. Analysis of electronic spectra shows that $Na_2MgGeCl_6$, Na_2MgGeI_6, $K_2MgGeCl_6$, and K_2MgGeI_6 exhibit indirect bandgap of 3.13 eV, 1.70 eV, 3.16 eV, and 1.72 eV, respectively. Mechanical analysis confirms that all the investigated compounds display ionic bonding nature, as evidenced by positive Cauchy pressure values and higher computed values of pugh's and poisson's ratios than 1.75 and 0.26, respectively, confirming their ductile behavior. The Zener Anisotropic "A_z" factors were also determined for the given compounds, highlighting their anisotropic behavior. Numerous optical parameters for instance dielectric functions, absorption coefficients, optical conductivity, refractive index and related features were analyzed and the findings indicate that all the titled compounds demonstrate excellent absorption, high conductivity, and minimal reflectivity. Among the investigated materials, only the I-based materials exhibited absorption peaks in the visible range. Moreover, I-based materials possess much lower effective masses and ensure their solidity for solar cell applications. In the UV region, all the investigated compounds exhibited intense peaks of absorption, with the highest peak noted for $K_2MgGeCl_6$ by achieving the value of 197.80×10^4 cm^{-1}. In the visible range, Na_2MgGeI_6 and K_2MgGeI_6 exhibited reflectivity values of 0.21, while in the UV range, reflectivity values for all the investigated compounds varied between 0.3 and 0.4.

Data Availability

Data will be made available on reasonable request

Conflict of interest

The authors declare that they have no known competing financial interests or personal relationships that could have appeared to influence the work reported in this paper.

1. J. Iqbal *et al*., Phase, microstructure, and microwave dielectric properties of a new ceramics system: (1-X) Mg(Ti0.95Sn0.05)O3 - XCaTiO3, *Ceramics International* **43** (2017) 14156, https://doi.org/10.1016/j.ceramint.2017.07.163
2. A. Kojima *et al*., Organometal halide perovskites as visiblelight sensitizers for photovoltaic cells, *J. Am. Chem. Soc*. **131** (2009) 6050, https://doi.org/10.1021/ja809598r
3. F. Deschler *et al*., High photoluminescence efficiency and optically pumped lasing in solution-processed mixed halide perovskite semiconductors, *J. Phys. Chem. Lett.* **5** (2014) 1421, https://doi.org/10.1021/jz5005285
4. A. Glushkova *et al*., Ultrasensitive 3D aerosol-jet-printed perovskite X-ray photodetector, *ACS Nano* **15** (2021) 4077, https://doi.org/10.1021/acsnano.0c10086
5. E. Y. Tiguntseva *et al*., Light-emitting halide perovskite

nanoantennas, *Nano Lett.* **18** (2018) 1185, https://doi.org/10.1021/acs.nanolett.7b04747

6. J. A. Sichert *et al*., Quantum size effect in organometal halide perovskite nanoplatelets, *Nano Lett.* **15** (2015) 6521, https://doi.org/10.1021/acs.nanolett.5b02985

7. M. Chen *et al*., 3D nanoprinting of perovskites, *Adv. Mater.* **31** (2019) 1904073, https://doi.org/10.1002/adma.201904073

8. M. Chen *et al*., Three-dimensional perovskite nanopixels for ultrahigh-resolution color displays and multilevel anticounterfeiting, *Nano Lett.* **21** (2021) 5186, https://doi.org/10.1021/acs.nanolett.1c01261

9. M. Kubicek, A. H. Bork, and J. L. Rupp, Perovskite oxides-a review on a versatile material class for solar-to-fuel conversion processes, *J. Mater. Chem. A* **5** (2017) 11983, https://doi.org/10.1039/C7TA00987A

10. R. Pandey *et al*., Mutual insight on ferroelectrics and hybrid halide perovskites: a platform for future multifunctional energy conversion, *Adv. Mater*. **31** (2019) 1807376, https://doi.org/10.1002/adma.201807376

11. W. J. Yin *et al*., Oxide perovskites, double perovskites and derivatives for electrocatalysis, photocatalysis, and photovoltaics, *Energy Environ. Sci.* **12** (2019) 442, https://doi.org/10.1039/C8EE01574K

12. J. Iqbal *et al*., Mg(Ti0.95Sn0.05)O3 - (Ca0.8Sr0.2)TiO3 ceramics: Phase, microstructure, and microwave dielectric properties, *J. Alloy. Compd*. **742** (2018) 107, https://doi.org/10.1016/j.jallcom.2018.01.279

13. G. García-Espejo- *et al*., Mechanochemical synthesis of three double perovskites: Cs2AgBiBr6, (CH3NH3)2TlBiBr6 and Cs2AgSbBr6, *Nanoscale* **11** (2019) 16650, https://doi.org/10.1039/C9NR04745G

14. W. Lee, S. Hong, and S. Kim, Colloidal synthesis of lead-free silver-indium double-perovskite Cs2AgInCl6 nanocrystals and their doping with lanthanide ions, *J. Phys. Chem. C* **123** (2019) 2665, https://doi.org/10.1021/acs.jpcc.8b10515

15. D. Bartesaghi *et al*., Charge carrier dynamics in Cs2AgBiBr6 double perovskite, *J. Phys. Chem. C* **122** (2018) 4809, https://doi.org/10.1021/acs.jpcc.7b12588

16. S. Yoon *et al*., Sb-substituted Cs2AgBiBr6 as much as it could be? -influence of synthesis methods on Sb-substitution level in Cs2AgBiBr6, *Energy Technol*. **10** (2022) 2200197, https://doi.org/10.1002/ente.202200197

17. A. Shatha *et al*., Investigation of electronic, optical, and thermoelectric features of X2ScAgCl6 (X = K, Na) double perovskites for renewable energy applications, *J. Solid State Chem.* **312** (2022) 123179, https://doi.org/10.1016/j.jssc.2022.123179

18. A. Ayyaz *et al*., Structural, morphological, elastic, optoelectronic, and thermoelectric properties of lead-free double perovskite Na2AgBiBr6 for photovoltaic applications: Experimental and DFT insight, *Ceramics International* **50** (2024) 15261, https://doi.org/10.1016/j.ceramint.2024.02.026

19. M. Shafiq *et al*., Ab initio study of lead-free double halide perovskite X2GeSnCl6 (X = Na K) compounds for energy conversion system, *Arabian J. Sci. Eng.* **49** (2024) 10061, https://doi.org/10.1007/s13369-023-08655-8

20. A. B. Siad *et al*., Elevating energy device potential: exploring optoelectronic and thermoelectric advantages in stable double perovskites K2NaInX6 (X = F, Cl, Br, I) via Ab initio analysis, *J. Mater. Sci*. **59** (2024) 1989, https://doi.org/10.1007/s10853-023-09279-8

21. M. H. Fahim, M. A. Rashid, and M. R. Amin, A comprehensive DFT study of the optoelectronic, mechanical, and thermoelectric properties of Rb2NaScCl6 double perovskite implying different pressure, *Mater. Today Commun.* **38** (2024) 108093, https://doi.org/10.1016/j.mtcomm.2023.108093

22. P. Blaha *et al*., WIEN2k: an augmented plane wave plus local orbitals program for calculating crystal properties, *Mater. Sci. Eng.* **1** (2001) 60.

23. J. P. Perdew, K. Burke, and M. Ernzerhof, Generalized gradient approximation made simple, *Phys. Rev. Lett.* **77** (1996) 3865, https://doi.org/10.1103/PhysRevLett.77.3865

24. F. Tran and P. Blaha, Accurate band gaps of semiconductors and insulators with a semilocal exchange-correlation potential, *Phys. Rev. Lett*. **102** (2009) 226401, https://doi.org/10.1103/PhysRevLett.102.226401

25. W. Kohn and L. J. Sham, Self-consistent equations including exchange and correlation effects, *Phys. Rev.* **140** (1965) A1133, https://doi.org/10.1103/PhysRev.140.A1133

26. T. Usman *et al*., First-principles study of structural, electronic, optical and thermoelectric properties of rare earth based perovskites XAlO3 (X = Sm, Eu, Gd), *Comput. Theor. Chem.* **1235** (2024) 114567, https://doi.org/10.1016/j.comptc.2024.114567

27. F. Birch, Finite elastic strain of cubic crystals, *Phys. Rev*. **71** (1947) 809, https://doi.org/10.1103/PhysRev.71.809

28. H. J. Monkhorst and J. D. Pack, Special points for Brillouin zone integrations, *Phys. Rev. B* **13** (1976) 5188, https://doi.org/10.1103/PhysRevB.13.5188

29. M. Jamal *et al*., IRelast package, *J. Alloys Compd*. **735** (2018) 569, https://doi.org/10.1016/j.jallcom.2017.11.085

30. M. D. Segall *et al*., First-principles simulation: ideas, illustrations and the CASTEP code, *J. Phys.: Condens. Matter* **14** (2002) 2717, https://doi.org/10.1088/0953-8984/14/11/301

31. C. J. Bartel *et al*., New tolerance factor to predict the stability of perovskite oxides and halides, *Sci. Adv.* **5** (2019) eaav0693, https://doi.org/10.1126/sciadv.aav0693

32. A. Ilyas *et al*., Investigation of the structural, electronic, magnetic and optical properties of CsXO3 (X = Ge, Sn, Pb) perovskites: A first-principles calculations, *Optik* **244** (2021) 167536, https://doi.org/10.1016/j.ijleo.2021.167536

33. Y. Dou *et al*., Boosted hydrogen evolution reaction for a nitrogen-rich azo-bridged metallated porphyrin network, *J. Colloid Interface Sci.* **650** (2023) 943, https://doi.org/10.1016/j.jcis.2023.07.054
34. S. J. Clark *et al*., First principles methods using CASTEP, Z. Kristallogr. - *Cryst. Mater.* **220** (2005) 567, https://doi.org/10.1524/zkri.220.5.567.65075
35. M. Manzoor *et al*., Tailoring the physical, optoelectronic and transport properties of novel lead-free sodium perovskites Na2TeX6 (X = Cl, Br, I) using DFT computation for photovoltaic and thermal devices, *Chinese J. Phys.* **89** (2024) 1333, https://doi.org/10.1016/j.cjph.2024.02.020
36. S. Kumari *et al*., Progress in theoretical study of lead-free halide double perovskite Na2AgSbX6 (X = F, Cl, Br, and I) thermoelectric materials, *J. Mol. Model.* **29** (2023) 195, https://doi.org/10.1007/s00894-023-05587-5
37. S. Nair *et al*., Cs2TlBiI6: a new lead-free halide double perovskite with direct band gap, *J. Phys.: Condens. Matter* **31** (2019) 445902, https://doi.org/10.1088/1361-648X/ab2f0e
38. M. Al-Yeamin *et al*., Study on pressure-induced band gap modulation and physical properties of direct band gap Ca3NX3 (X = Cl, Br) for optoelectronic and thermoelectric applications, *Surfaces and Interfaces* **56** (2025) 105559, https://doi.org/10.1016/j.surfin.2024.105559
39. L. K. Ono, E. J. J. Perez, and Y. Qi, Progress on Perovskite Materials and Solar Cells with Mixed Cation and Halide Compositions, *ACS Appl. Mater. Interfaces* **9** (2017) 30197, https://doi.org/10.1021/acsami.7b06001
40. L. Whalley *et al*., Impact of non-parabolic electronic band structure on the optical and transport properties of photovoltaic materials, *Phys. Rev. B* **99** (2019) 085207, https://doi.org/10.1103/PhysRevB.99.085207
41. N. A. Noor *et al*., Analysis of direct band gap A2ScInI6 (A = Rb, Cs) double perovskite halides using DFT approach for renewable energy devices, *J. Mater. Res. Technol.* **13** (2021) 2491, https://doi.org/10.1016/j.jmrt.2021.06.032
42. S. Wu *et al*., The evolution and future of metal halide perovskite-based optoelectronic devices, *Matter* **4** (2021) 3814, https://doi.org/10.1016/j.matt.2021.09.013
43. T. Usman *et al*., GGA and GGA + U Study of Rare Earth- Based Perovskites in Cubic Phase, *J. Supercond. Nov. Magn.* **30** (2017) 1389, https://doi.org/10.1007/s10948-016-3946-3
44. M. Y. Sofi, M. S. Khan, and M. A. Khan, Control of Spin on ferromagnetism and thermoelectric properties of K2GeMnX6 (X = Cl, Br, I) halide perovskites: emerging candidate for semiconductor spintronics and thermoelectric applications, *Mater. Adv.* **5** (2024) 4913, https://doi.org/10.1039/D4MA00176D
45. P. K. Kamlesh *et al*., First principles calculations of inherent properties of Rb based state of the art half Heusler compounds: promising materials for renewable energy applications, *Phys. Scr.* **96** (2021) 115802, https://doi.org/10.1088/1402-4896/ac1f8f
46. G. Murtaza and I. Ahmad, First principle study of the structural and optoelectronic properties of cubic perovskite CsPbM3 (M = Cl, Br, I), *Physica B* **406** (2011) 3222, https://doi.org/10.1016/j.physb.2011.05.038
47. M. A. Rehman *et al*., Study of physical properties of Cs2TlGaX6 (X = Cl, Br) halide perovskites via HSE-06 hybrid technique for high efficiency solar cells, *Opt. Quantum Electron.* **56** (2024) 1079, https://doi.org/10.1007/s11082-024-05427-0
48. M. Rashid, Study of Vanadium Difluoride AVF3 (A = Na, K, Rb) for optoelectronic and thermoelectric device applications via ab initio calculations, *J. Supercond. Nov. Magn.* **33** (2020) 1167, https://doi.org/10.1007/s10948-019-05309-7
49. M. Hussain *et al*., Systematic study of optoelectronic and transport properties of cesium lead halide (Cs2PbX6; X = Cl, Br, I) double perovskite for solar cell applications, *Ceramics International* **46** (2020) 21378, https://doi.org/10.1016/j.ceramint.2020.05.219